

A Performance Study of Variational Quantum Algorithms for Solving the Poisson Equation on a Quantum Computer

Mazen Ali^{1,*} and Matthias Kabel^{1,†}

¹*Fraunhofer ITWM, 67663 Kaiserslautern, Germany*

Recent advances in quantum computing and their increased availability has led to a growing interest in possible applications. Among those is the solution of partial differential equations (PDEs) for, e.g., material or flow simulation. Currently, the most promising route to useful deployment of quantum processors in the short to near term are so-called hybrid variational quantum algorithms (VQAs). Thus, variational methods for PDEs have been proposed as a candidate for quantum advantage in the noisy intermediate scale quantum (NISQ) era. In this work, we conduct an extensive study of utilizing VQAs on real quantum devices to solve the simplest prototype of a PDE – the Poisson equation. Although results on noiseless simulators for small problem sizes may seem deceptively promising, the performance on quantum computers is very poor. We argue that direct resolution of PDEs via an amplitude encoding of the solution is not a good use case within reach of today’s quantum devices – especially when considering large system sizes and more complicated non-linear PDEs that are required in order to be competitive with classical high-end solvers.

I. INTRODUCTION

The technological progress in quantum computing has spurred a lot of research into applications with the potential for an advantage over classical computing. One of these possible applications is the solution of partial differential equations (PDEs) that are extensively used in various areas of engineering such as computational fluid dynamics (CFD) [1] or material simulation [2, 3].

In its simplest form, a linear PDE is transformed via a discretization method into a system of linear equations. The latter can then be solved with the quantum HHL method [4]. For general linear PDEs in three spatial dimensions, one can expect at best a quadratic speedup compared to classical solvers, see [5]. The speedup may, however, increase for high-dimensional PDEs. Despite recent progress with HHL [6–8], it requires deep entangling circuits and has thus limited scalability within the noisy intermediate scale quantum (NISQ) era computers.

A more NISQ friendly alternative are so-called (*hybrid*) *variational algorithms*. These are (mostly heuristic) methods that rely on a quantum-classical approach where the quantum computer is only used to execute relatively shallow circuits to estimate cost functionals within a classical optimization loop. Hybrid methods have gained a lot of attention [9] as *the* class of methods for NISQ devices, including applications to PDEs [10–12].

The simplest example of a model PDE problem is the 2nd order linear Poisson equation. This has been previously addressed in [10, 11] using the hybrid variational quantum linear solver (VQLS) from [13] with experiments on simulators. In this work, we conduct a thorough study of the applicability of variational hybrid methods to PDEs by performing extensive tests with VQLS for the Poisson equation on both simulators with statistical

finite sampling (shot) noise and real quantum hardware using superconducting qubits [14].

Our results indicate that hybrid solvers for PDEs are not a promising route for achieving quantum advantage in the short to near term. It is well known that, when increasing system size, a) PDEs require preconditioning and b) variational algorithms suffer from barren plateaus. Neither of these issues are present for the system sizes considered in this work. Nonetheless, VQLS struggles to converge (fast) even for small system sizes – both on quantum hardware and simulators with shot noise – in the absence of a), b), data encoding and readout issues. Moreover, the competition – namely classical PDE solvers – can typically achieve precision that seems beyond the reach of quantum algorithms relying on finite sampling.

A common argument *for* the potential of quantum advantage is the scalability with respect to the number of spatial dimensions of the PDE – ignoring data en- and decoding, there is no apparent “curse of dimensionality” in VQLS applied to, e.g., the Poisson equation [15]. However, for interesting system sizes of $n \geq 20$ qubits and the resulting increase in noise, we believe other classical methods for high-dimensional PDEs [16–18] are more promising than VQAs. While there still may be some benefit in using NISQ devices for, e.g., material simulation or CFD, we believe it does not lie within the direct resolution of PDEs via an amplitude encoding of the solution (see Section III).

Finally, we mention that in this work we considered several but not all error mitigation techniques. Particularly noteworthy is probabilistic error cancellation (PEC) [19, 20] that was recently added to IBM’s runtime service. PEC attempts to produce unbiased estimates of expectation values by fitting a (sparse) Pauli noise model to the physical noise on the quantum device and implementing the inverse of said noise channels by sampling randomized Pauli twirled circuits. The success of this denoising method depends on several non-trivial assumptions

* mazen.ali@itwm.fraunhofer.de

† matthias.kabel@itwm.fraunhofer.de

about the quality of the noise model and involves an exponential sampling overhead. It is a potentially interesting research question whether PEC would benefit the estimation of observables described in this work and if it would scale to large system sizes.

The remainder of the paper is organized as follows. In Section II, we introduce the Poisson equation and the different ways to estimate the Poisson operator on a gate based quantum computer. In Section III, we go over some basics of VQLS and the different cost functions used for optimization. In Section IV, we test individual components of VQLS for the Poisson equation – both on simulators and quantum hardware – and conclude with the overall performance of the VQLS optimization in the presence of noise.

II. POISSON EQUATION

The Poisson equation with Dirichlet boundary conditions is defined as

$$\begin{aligned} -\nabla^2 u(x) &= f(x) & \text{for } x \in \Omega, \\ u(x) &= 0 & \text{for } x \in \partial\Omega, \end{aligned}$$

for an open domain $\Omega \subset \mathbb{R}^d$ with Lipschitz boundary $\partial\Omega$ and real-valued $u : \Omega \rightarrow \mathbb{R}$ and $f : \Omega \rightarrow \mathbb{R}$. The weak (variational) form of this equation reads: find $u \in H_0^1(\Omega)$ that satisfies

$$\begin{aligned} a(u, v) &:= \int_{\Omega} \nabla u(x) \cdot \nabla v(x) \, dx \\ &= \int_{\Omega} f(x)v(x) \, dx =: f(v), \end{aligned}$$

for all $v \in H_0^1(\Omega)$, where $H_0^1(\Omega)$ is the space of all weakly differentiable L^2 -functions that are zero on $\partial\Omega$ in the trace sense.

In the finite element method (FEM), one discretizes the Poisson equation by choosing a set of basis (*test* and *trial*) functions

$$V_h := \{\varphi_k : k = 0, \dots, N-1\} \subset H_0^1(\Omega),$$

and, consequently, the *discrete* Poisson equation reads: find $\mathbf{u} = (u_k)_{k=0}^{N-1}$ such that $u_h := \sum_{k=0}^{N-1} u_k \varphi_k$ and

$$a(u_h, v_h) = f(v_h), \quad \text{for all } v_h \in V_h,$$

or, equivalently, solve

$$\begin{aligned} \mathbf{A}\mathbf{u} &= \mathbf{f}, \\ \mathbf{A} &:= (a(\varphi_j, \varphi_i))_{i,j=0}^{N-1}, \\ \mathbf{f} &:= (f(\varphi_i))_{i=0}^{N-1}. \end{aligned} \tag{1}$$

In this work, we test the simplest case $d = 1$, $\Omega = (0, 1)$ and piecewise linear FEM. Therefore, \mathbf{A} is a tridiagonal

matrix with 2's on the main diagonal and -1 's on the off-diagonals

$$\mathbf{A} = \frac{1}{h} \begin{pmatrix} 2 & -1 & 0 & \dots \\ -1 & 2 & -1 & \dots \\ & & \ddots & \\ & & & -1 & 2 \\ & & & & -1 & 2 \end{pmatrix}, \tag{2}$$

where $h = \frac{1}{N+1}$ denotes the mesh size (distance between discretization nodes). Alternatively, one can re-scale the domain Ω to $(0, N+1)$, in which case $h = 1$.

For the right-hand-side (RHS) \mathbf{f} , we consider the two border cases where \mathbf{f} is constant and where \mathbf{f} contains a discontinuous jump. The constant case leads to a smooth solution u whereas the discontinuous case leads to a singularity (in the derivatives) of u . While this significantly impacts the performance of classical methods (or requires special techniques such as, e.g., adaptive or hp-methods), the discontinuity has no substantial effect on the training in Section IV. Both cases can be approximated as quantum states on n qubits with the following unitaries

$$\begin{aligned} |\mathbf{f}_C\rangle &:= H^{\otimes n} |0\rangle_n, & (\text{Hn}) \\ |\mathbf{f}_D\rangle &:= H^{\otimes n-1} \otimes X |0\rangle_n, & (\text{HnX}) \end{aligned}$$

where H and X are the Hadamard and Pauli- X gates, respectively.

We cast the LSE problem from (1) to a problem of determining a quantum state via an amplitude encoding as follows. Find an n -qubit quantum state $|\mathbf{u}\rangle = \frac{1}{\|\mathbf{u}\|} \sum_{k=0}^{2^n-1} u_k |k\rangle$ that satisfies

$$(\|\mathbf{u}\|)\mathbf{A}|\mathbf{u}\rangle = (\|\mathbf{f}\|)|\mathbf{f}\rangle. \tag{3}$$

We re-scale such that $h\|\mathbf{f}\| = 1$ for simplicity and since this does not affect conclusions about the overall performance of VQLS.

Within a variational solver, one uses a parametrized ansatz $|\psi(\theta)\rangle$ and optimizes over the parameters $\theta = (\theta_1, \dots, \theta_p)$ to approximate the normalized solution $|\mathbf{u}\rangle \approx |\psi(\theta^*)\rangle$. To this end, we must estimate terms such as $\langle \psi(\theta) | \mathbf{A} | \psi(\theta) \rangle$ on a quantum computer. There are several ways of estimating the observable \mathbf{A} : details of all decompositions used in this work are provided in Fig. 14 – 17.

The simplest option is decomposing \mathbf{A} into Pauli strings. This requires $\mathcal{O}(2^n)$ terms and, consequently, any potential quantum advantage is lost. Another option was presented in [11], where \mathbf{A} is decomposed into $\mathcal{O}(n)$ simple operators, see Fig. 16. Note that, however, the decomposition terms in Liu21 commute and can be thus grouped together into $\mathcal{O}(1)$ terms, see Fig. 17. Finally, in [10], yet another decomposition method was proposed with $\mathcal{O}(1)$ terms.

While all of these decompositions are mathematically equivalent, they have a trade-off between number of circuits to run vs. entangling gates required for each circuit.

The matrix \mathbf{A} from (2) can be decomposed as

$$\mathbf{A} = 2I^{\otimes n} - I^{\otimes n-1} \otimes X + R. \quad (4)$$

The expectation of the first term is constantly equal to 2. The second term requires adding only one Hadamard gate on the least significant qubit [21], i.e., here the accuracy will mostly depend on the gates required for the ansatz $|\psi(\theta)\rangle$. The remaining term R (off-diagonal -1 's on odd positions) requires either exponentially many Pauli strings or one highly entangling circuit, see also Fig. 15, 17. On one hand, using highly entangling unitaries, the estimation of the expectation value of R is inaccurate on today's quantum computers. On the other hand, as we will see in Section IV D, the expectation value of \mathbf{A} is dominated by the constant part. This is a good example of an abstract mathematical problem that is deceptively simple to solve classically, but is rather complicated to run on a modern day quantum computer.

III. VQLS COST FUNCTIONS

VQLS was first introduced in [13]. It is an extension of the variational quantum eigensolver [22], where one uses a parametrized ansatz function $|\psi(\theta)\rangle$ and minimizes the expected energy of some Hamiltonian. The different types of ansatz used in this work are detailed in Fig. 12.

For linear systems, the authors in [13] propose Hamiltonians for which the ground state corresponds to the normalized solution state from (3). One can also minimize more general cost functions that do not directly correspond to Hamiltonian minimization, e.g., as for the cost function in [10]. In this work, we will use one of the following four cost functions

$$\begin{aligned} C_N(\theta) &:= -\frac{1}{2} \frac{(\Re \langle \mathbf{f} | \psi(\theta) \rangle)^2}{\langle \psi(\theta) | \mathbf{A} | \psi(\theta) \rangle}, \\ C_{NN}(\theta, s) &:= \frac{1}{2} s^4 \langle \psi(\theta) | \mathbf{A} | \psi(\theta) \rangle - s^2 \Re \langle \mathbf{f} | \psi(\theta) \rangle, \\ C_G(\theta) &:= \frac{\langle \psi(\theta) | H_G | \psi(\theta) \rangle}{\langle \psi(\theta) | \mathbf{A}^\dagger \mathbf{A} | \psi(\theta) \rangle}, \\ C_L(\theta) &:= \frac{\langle \psi(\theta) | H_L | \psi(\theta) \rangle}{\langle \psi(\theta) | \mathbf{A}^\dagger \mathbf{A} | \psi(\theta) \rangle}, \end{aligned} \quad (5)$$

where, for $|\mathbf{f}\rangle = U_f |0\rangle$,

$$\begin{aligned} H_G &:= \mathbf{A}^\dagger U_f (I^{\otimes n} - |0\rangle\langle 0|) U_f^\dagger \mathbf{A}, \\ H_L &:= \mathbf{A}^\dagger U_f \left(I^{\otimes n} - \frac{1}{n} \sum_{j=0}^{n-1} |0_j\rangle\langle 0_j| \otimes I_j \right) U_f^\dagger \mathbf{A}, \end{aligned}$$

with $|0_j\rangle\langle 0_j|$ being the projection onto the j -th qubit only and I_j the identity on all except the j -th qubit. The operational meaning, pros and cons of different cost functions have been previously discussed in other works [13, 23, 24]. The cost functions C_G and C_L determine

the solution by minimizing the residual $\mathbf{f} - \mathbf{A}|\psi(\theta)\rangle$ (disregarding re-scalings), while C_N and C_{NN} minimize the Dirichlet energy of the solution candidate.

Cost functions C_G and C_L were introduced in [13]. C_N was introduced in [10] and corresponds to the Dirichlet energy for the normalized solution, while C_{NN} is its non-normalized version, i.e., s^2 stands for the norm of \mathbf{u} . Although the global minimum of all four cost functions corresponds to the normalized solution of (3), the estimation accuracy and convergence of optimizers varies. Moreover, we note that the cost functions C_N and C_{NN} require fewer and simpler circuits than C_G and C_L .

IV. RESULTS

A VQLS setup consists of choosing the type of ansatz, the RHS, the number of qubits and layers of the ansatz, the cost function, the classical optimization method and the estimation backend. In Section IV A, we probe the expressivity and trainability of different ansatzes and cost functions by testing on noiseless state-vector simulators, i.e., in the absence of both hardware noise and statistical finite sampling (shot) noise. In Section IV B, we test the fidelity of different ansatzes both on simulators with shot noise and on different IBM backends. In Section IV C, we test the accuracy of estimating inner products. In Section IV D, we test the accuracy of estimating the Poisson operator expectation. In Section IV E, we test the accuracy of estimating different cost functions. In Section IV F, we test the cosine similarity of estimating gradients. Finally, in Section IV G, we test the overall performance of several optimizers with different cost functions. The tests in Sections IV B – IV F were performed on a sample of randomly generated ansatz parameters, where we compared, e.g., different error percentiles.

A. Training Without Noise

In this section, we estimate all quantities on a state-vector simulator, i.e., numerically exact and choose the BFGS optimizer [25–28]. It was observed both in previous work [29] and our own experiments that BFGS performs best on small variational problems in the absence of noise. We run each VQLS setup for 15 randomly generated initial values and select the best run based on the smallest observed cost function value. We use the same set of random initial values across all experiments.

In Fig. 1, we display the solution fidelity for the minimization based on the four different cost functions from (5), for varying number of qubits and ansatz layers. The cost function C_N leads to the fastest convergence. The non-normalized version C_{NN} displays similar but slightly worse behavior. Our main reason for considering C_{NN} is a better behavior in the presence of noise, as we will see in the following sections. The global and local cost func-

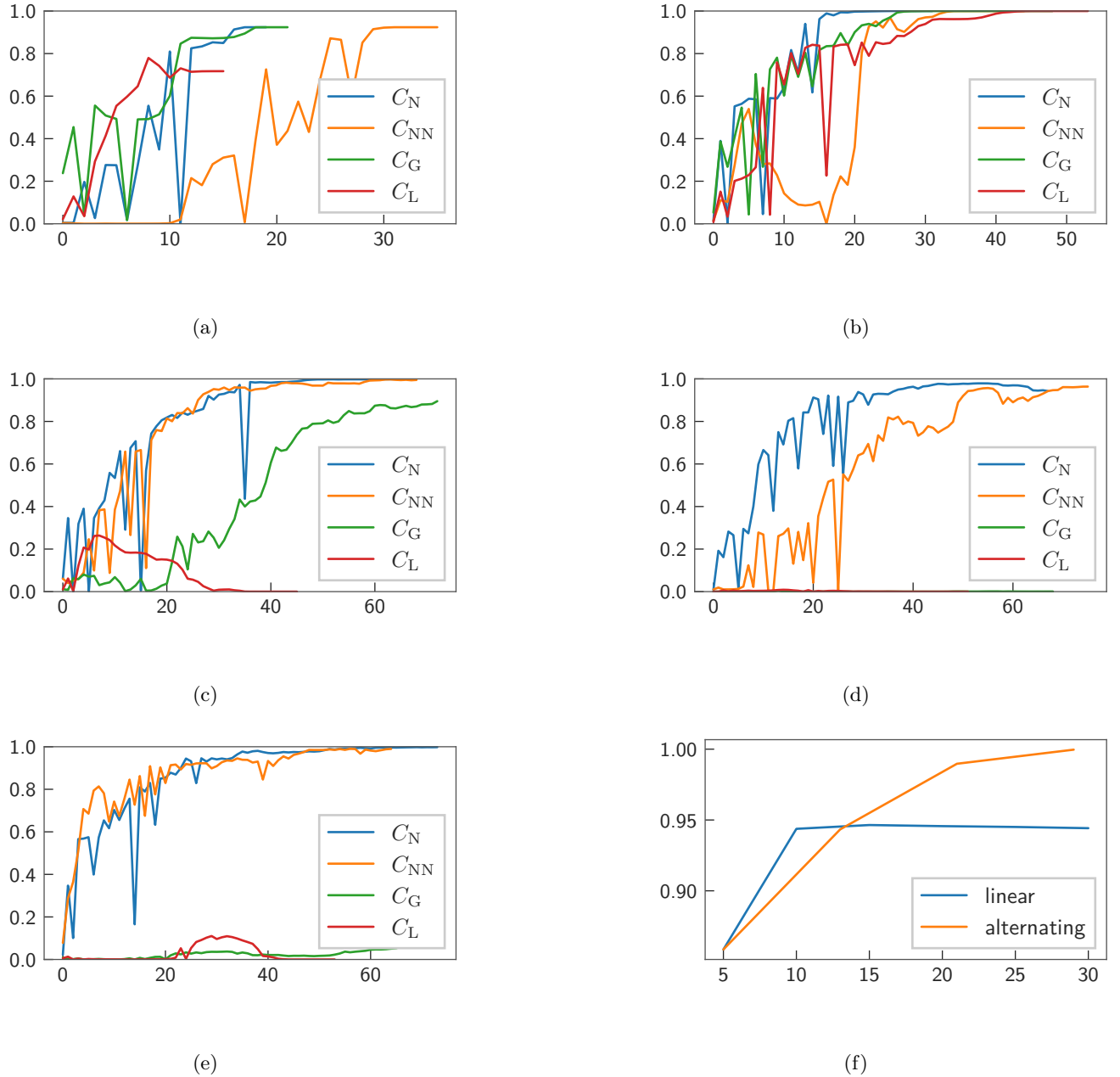


Figure 1: Solution fidelity vs. number of cost function evaluations. Note that we display *all* cost evaluations, i.e., not only cost for current (accepted) iterate θ_k . RHS (HnX), BFGS optimizer, state vector simulator (no noise). (a) Ansatz linear alternating R_Y - CZ (see Fig. 12), $n = 3$, $l = 0$. (b) Ansatz linear alternating R_Y - CZ , $n = 3$, $l = 3$. (c) Ansatz linear alternating R_Y - CZ , $n = 5$, $l = 3$. (d) Ansatz linear alternating R_Y - CZ , $n = 8$, $l = 3$. (e) Ansatz linear alternating R_Y - CZ ansatz, RHS (Hn), $n = 5$, $l = 3$. (f) Final solution fidelity vs. number of ansatz parameters, RHS (HnX), $n = 5$, R_Y - CZ ansatz, linear vs linear alternating.

tions, C_G and C_L , fail to converge at a relatively small number of qubits and are, in addition, more costly to estimate than C_N and C_{NN} .

The choice of the RHS does not pose a problem for the C_N and C_{NN} cost functions. For C_G and C_L , the barren plateaus worsen for the RHS (Hn). This may seem counter-intuitive from the perspective of classical PDE

methods, where smoother data is generally associated with better convergence. For VQLS, however, particular combinations of ansatz and RHSs can lead to very flat optimization landscapes or even constant cost functions. The choice of alternating vs. non-alternating entanglement pattern from Fig. 12 has a significant impact on the final solution fidelity.

B. Ansatz Fidelity

Having computed the optimal parameters, how accurately can we sample the corresponding distribution from the quantum device? In this section, we test the fidelity of different ansaetze across multiple backends. As a benchmark, we will use the sampling error of a simulator with shot noise. The different ansatz architectures are described in Fig. 12.

In Fig. 2a, we see that the median fidelity is quite close to the noiseless quantum simulator up to 10 qubits. Adding entangling layers at 10 qubits reduces the fidelity significantly. Comparing the different backends, the performance is similar, with dips in fidelity observed on either newer backends or on small backends where we exhausted the maximum number of qubits.

In Fig. 2b, we compare different ansatz architectures. Some results are to be expected, e.g., adding periodic entanglement (CNOTs on first and last qubit) leads to more CNOTs post transpilation – since the topology of IBM devices does not natively accommodate such entanglement (see Fig. 18) – and, hence, lowers fidelity. Other results are, however, less intuitive. For example, linear R_X - CX performs slightly better than linear R_Z - CX , even though R_Z rotations are native to IBM hardware. More notably, linear $U3$ - CX (all 3 rotations) performs best despite performing more rotations. The number of parameters is tripled for $U3$, i.e., for $p = 180$, $U3$ - CX has as many entangling layers as R_Y - CZ for $p = 60$.

In Fig. 2c, we consider the fidelity behavior when increasing the number of shots (measurement samples). The convergence on a noiseless quantum simulator and `ibmq_ehningen` are similar with a constant offset due to hardware noise. For the simulator, the number of entangling layers does not affect the fidelity, as expected, whereas for the real backend adding layers accumulates hardware error.

Finally, when executing circuits on a real backend, one has various transpilation and error mitigation options. For comparison, we select those options that we consider to be relatively generic and easy to run by most users [30]. For transpilation, we compare no optimization with `Qiskit`'s swap-optimized transpilation based on the SABRE heuristic [31]. Due to the stochastic nature of this heuristic, we transpile 20 times and select the circuit minimizing a weighted average of depth and number of CNOTs, with number of CNOTs having twice the weight. For error mitigation (EM), we test either no EM, matrix-free measurement EM (MEM) [32], simple XX dynamic decoupling (DD) with as-late-as-possible instruction scheduling or noise aware transpilation (the `mapomatic` tool from [33]). The results are summarized in Fig. 2d.

Optimized transpilation and measurement error mitigation consistently improve fidelity. When an algorithm does not change the topology of input circuits, transpilation has to be performed only once and, thus, the overhead is negligible. For MEM, one has to perform regular

calibrations on the target backend. If integrated into the output pipeline, the overhead for MEM can be negligible as well.

The results for dynamic decoupling are less clear. From Fig. 2d, 13 and other experiments not illustrated here, we observed that it can both improve and worsen the results. We are not aware of a universal DD method that works on any circuit, it is still an active area of research and a more problem-tailored DD method might be required for consistent improvement (see, e.g., [34]).

The same conclusion applies to noise aware transpilation from [33]. Here, a better choice of cost function than the default for selecting less noisy qubits might improve results. We do not investigate this further.

C. Inner Products

Estimating inner products is a basic numerical subroutine required by any linear solver. In our case, we estimate inner products of the form $\Re \langle \mathbf{f} | \psi(\theta) \rangle$. This is typically done via the Hadamard test as in [10, 13]. For the special case of the cost function C_N from (5) and an ansatz with only real-valued amplitudes, we can estimate $|\langle \mathbf{f} | \psi(\theta) \rangle|^2$ by measuring the overlap, which requires fewer controlled gates than the Hadamard test. The overlap test measures all qubits as opposed to one qubit for the Hadamard test. We compare relative errors since the exact value of $\Re \langle \mathbf{f} | \psi(\theta) \rangle$ is often quite small and thus small absolute errors are not informative.

In Fig. 3a – 3d, we compare the different methods w.r.t. the number of layers and shots with references to the exact value $|\langle \mathbf{f} | \psi(\theta) \rangle|^2$. The conclusions are different depending whether one considers only the median or the mean. The overlap test performs slightly better if one ignores outliers and vice versa for the Hadamard test. For the median, results do not improve significantly for more than 1000 shots, for the mean, the threshold seems to be 10000 shots for the Hadamard test.

In Fig. 3e, we consider different quantum amplitude estimation (QAE) techniques. Maximum likelihood quantum amplitude estimation (MLQAE) improves accuracy. Note, however, that inner product estimation within VQLS is applied as a subroutine several times per optimizer step. Therefore, on today's quantum computing hardware, the additional overhead for adding QAE to each subroutine call is substantial for the overall training, while the accuracy gain is potentially negligible.

Finally, in Fig. 3f, we consider adding different error mitigation techniques. Unlike in Section IV B, the mean relative error is smallest when applying all error mitigation techniques, while applying only optimized transpilation with measurement error mitigation performs almost as well.

Although there is a lot of variability in errors depending on ansatz architecture, RHS, number of layers and error mitigation techniques – in all cases the relative error for estimating the basic quantity $\Re \langle \mathbf{f} | \psi(\theta) \rangle$ is very

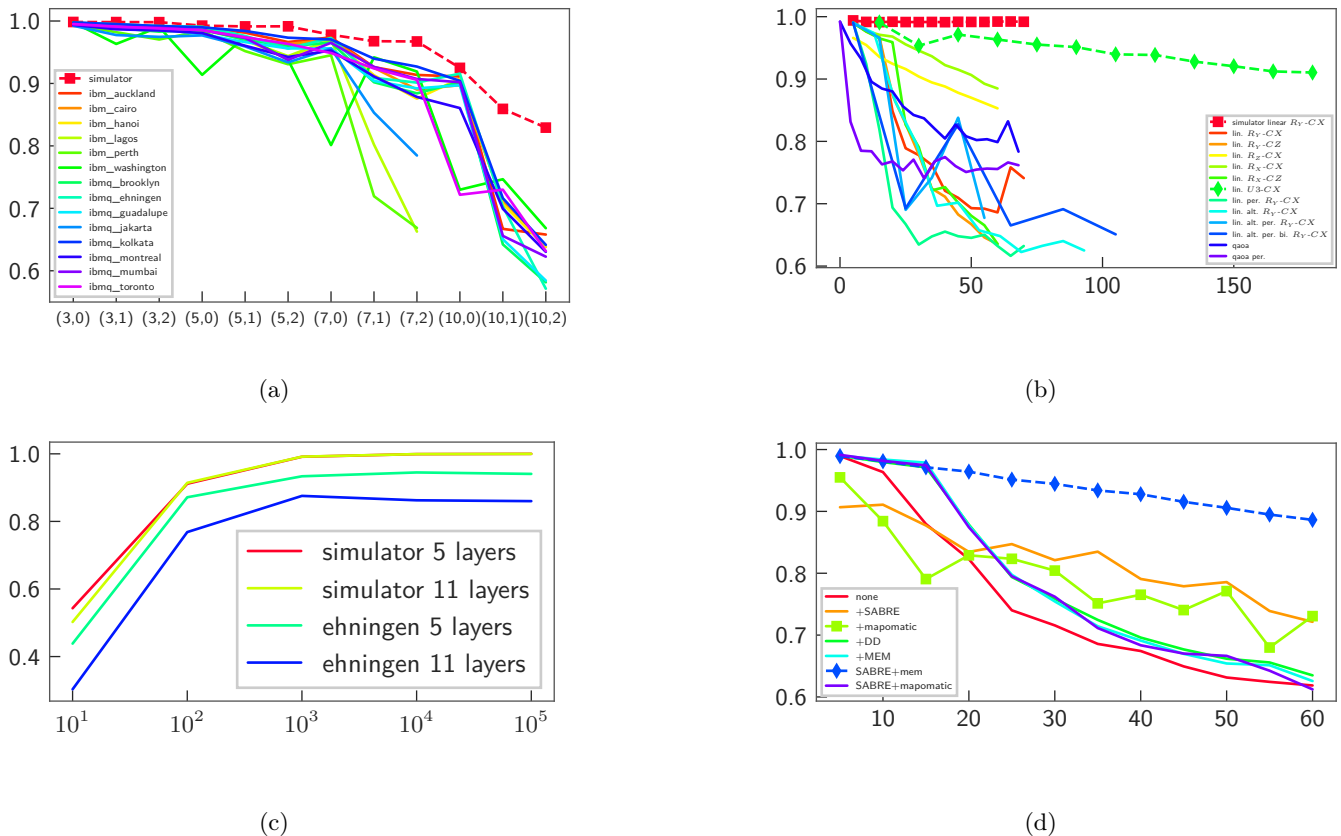


Figure 2: Experiments with ansatz fidelity on real backends. Median fidelity out of 50 random parameter samples. For (a) – (c) only optimized transpilation was applied. (a) Median fidelity vs. (qubits = n , layers = l), number of parameters = $n \cdot l$, on different IBM backends. 1000 shots. (b) Fidelity vs. number of parameters for different ansatz architectures with 5 qubits on `ibmq_ehningen`. 1000 shots. See Fig. 12 for details on ansatz architectures. (c) Fidelity vs. number of shots for the linear R_Y-CZ ansatz with 5 qubits. (d) Fidelity vs. number of parameters for different transpilation and error mitigation heuristics, linear R_Y-CZ ansatz with 5 qubits.

large, even on simulators. Furthermore, inner product estimation is a basic subroutine that would be required to estimate functionals of the solution such as, e.g., taking the average of \mathbf{u} , and this is a necessary step to gain any sort of quantum advantage for PDE solvers [5]. Based on our experiments, even if the solution $|\mathbf{u}\rangle$ is accurately approximated on a quantum device via $|\psi(\theta)\rangle$, the necessary accuracy for estimating $\langle r|\psi(\theta)\rangle$ for some functional r and $n \geq 20$ qubits translate into a very large number of shots together with high requirements for hardware fidelity and error mitigation that may be unrealistic in the near term.

D. Operator Expectation

In this section, we test the accuracy of estimating $\langle \psi(\theta)|\mathbf{A}|\psi(\theta)\rangle$. As discussed in Section II, there are at least four different ways to estimate \mathbf{A} , refer to Fig. 14 – 17 for the different decompositions.

In Fig. 4, we compare the relative errors. At first

glance, this estimation seems to perform much better than inner product estimation from Section IV C. However, this is mainly due to the “constant” part of \mathbf{A} , see (4), $\langle \psi(\theta)|\mathbf{A}|\psi(\theta)\rangle \approx 2$.

Fig. 4c shows that most of the error is hardware noise, e.g., for $q = 5$, $l = 3$ it is not worth going beyond 100 – 1000 shots. Fig. 4d shows the number of CNOTs required for the different decomposition methods. Together with Fig. 4c, the Liu21 decomposition (see Fig. 16) performs best. We do not consider using the Pauli decomposition a viable option since it does not scale. Recall that the number of observables for Liu21 scales linearly with the number of qubits as opposed to constant for Sato21 and Liu21Grouped.

E. Cost Functions

In this section, we compare the accuracy of estimating C_N and C_{NN} from (5). For inner product estimation, we use the Hadamard test, and, for operator expectation, we

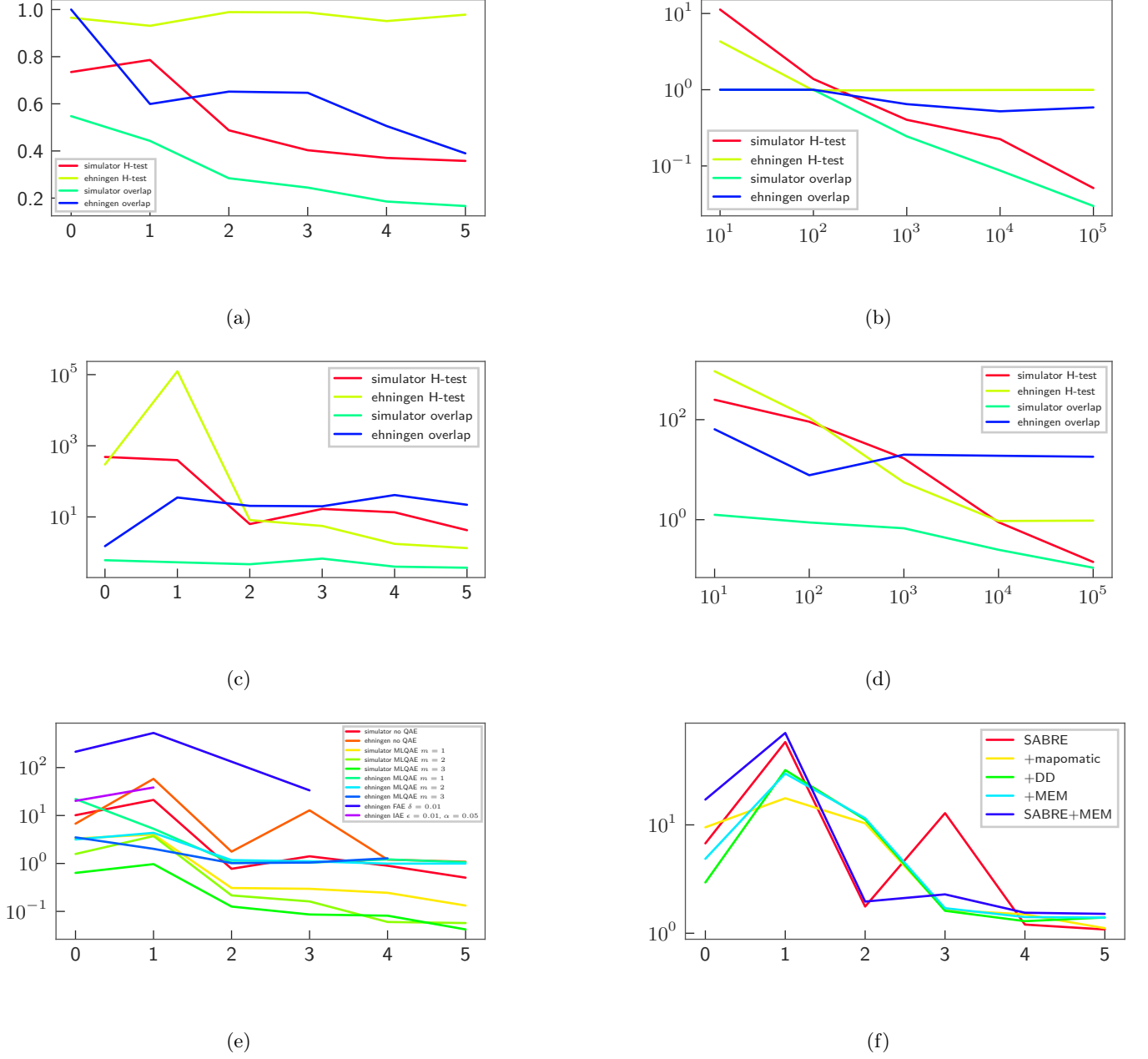


Figure 3: Relative error inner product estimation. 50 parameter samples in all plots. (a) Median relative error vs. number of layers, $n = 5$ qubits, linear R_Y - CZ ansatz, RHS (Hn), 1000 shots. (b) Median relative error vs. number of shots, 5 qubits and 3 layers, linear R_Y - CZ ansatz, RHS (Hn), 1000 shots. (c) Same as (a) but mean instead of median. (d) Same as (b) but mean instead of median. (e) Mean relative error vs. number of layers for different QAE methods, R_Y - CZ ansatz, 5 qubits, RHS (Hn). (f) Mean relative error vs. number of layers for different error mitigation techniques, R_Y - CZ ansatz, 5 qubits, RHS (Hn).

use the Liu21 decomposition.

In Fig. 5a, we compare the accuracy w.r.t. the number of shots. Unlike before, we show a more detailed comparison here including the $p = 0, 5, 25, 50, 75, 95, 100$ error percentiles. We see that the accuracy saturates at about $S = 1000$ shots. Moreover, estimation of C_{NN} is slightly more accurate.

Next, we test if the mean absolute error in cost function estimation is larger than the mean variation of exact cost function values. This should indicate if an optimizer can detect a descent direction in the presence of hardware noise. We estimate the variation as follows. Generate a sample of 50 random parameters $\Omega := \{\theta^1, \dots, \theta^{50}\}$. Then, for each parameter in Ω , sample 100 random pa-

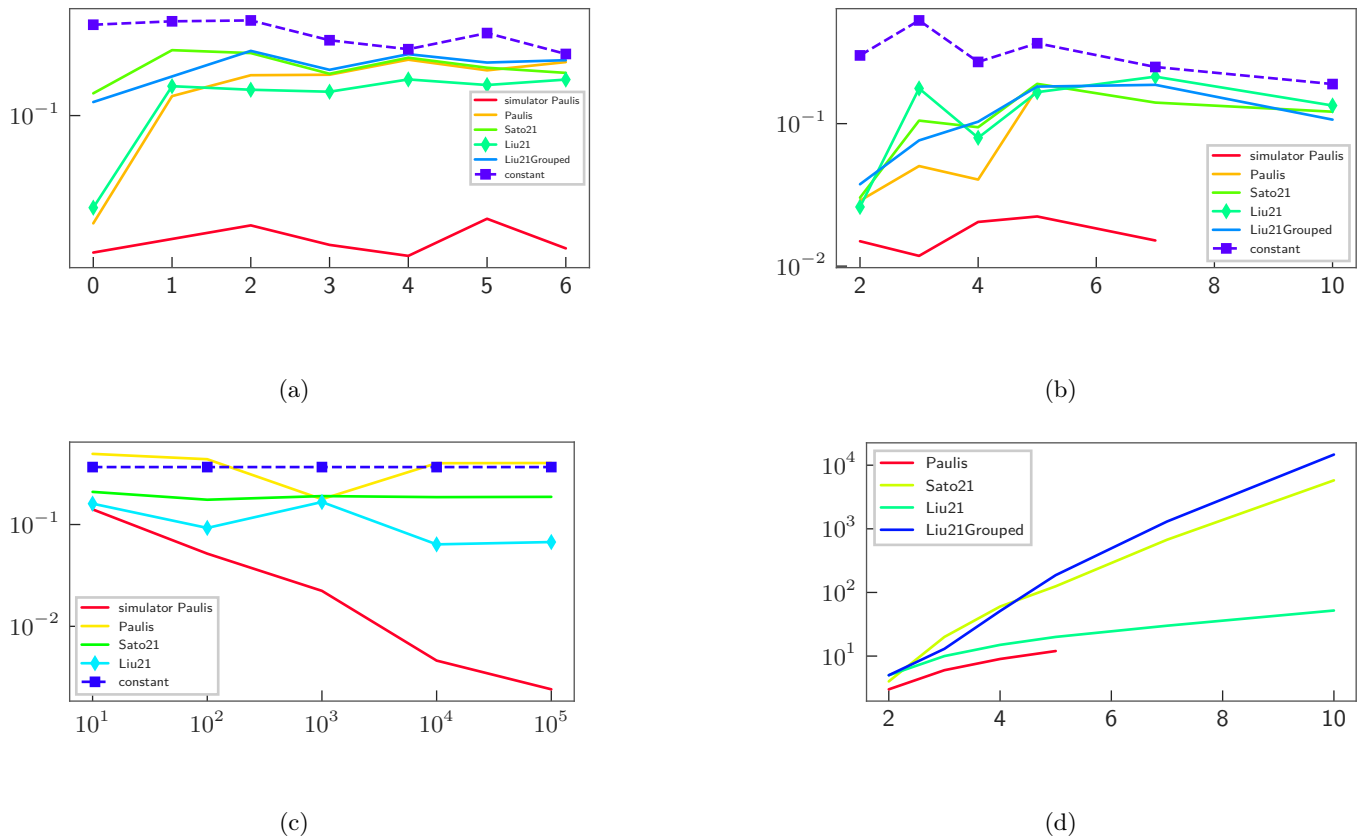


Figure 4: 50 parameter samples in (a) – (c). (a) Mean relative error vs. number of layers, linear R_Y -CZ, 5 qubits, 1000 shots. (b) Mean relative error vs. number of qubits, linear R_Y -CZ, 3 layers, 1000 shots. (c) Mean relative error vs. number of shots, linear alternating R_Y -CZ. (d) Number of CNOTs vs. number of qubits, linear alternating R_Y -CZ, 3 layers.

rameters $\Delta(\theta) := \{\delta^1(\theta), \dots, \delta^{100}(\theta)\}$, where each of the components of $\delta^k(\theta)$ is between -2π and 2π . Select a step size and compute the variations

$$\text{var}(\theta, \delta) := |C(\theta) - C(\theta + \text{step} \cdot \delta)|,$$

for each δ in $\Delta(\theta)$ and each θ in Ω . In total, we thus have differences of cost function values sampled at 500 different points.

The results are summarized in Fig. 5b – 5d. In both cases the estimation is quite noisy as the absolute error in cost function value is within the range of cost function variation. Thus, in general, it is unclear if an optimizer can recognize a descent direction in such a noisy regime.

The results for C_{NN} are slightly better. This is mostly due to the norm parameter s in (5). We thus expect that, for random initial values, an optimizer would at first perform better for C_{NN} . However, as the optimization progresses and the value of s is improved, C_{NN} should encounter the same noise issues as C_{N} .

F. Gradients

In this section, we test the cosine similarity of estimated vs. exact gradients for C_{N} and C_{NN} . The cosine similarity of two vectors x and y is defined as $\langle x|y \rangle / (\|x\| \|y\|)$. The results are summarized in Fig. 6.

Per optimizer iteration, often several calls of gradient estimation are required. For each gradient call, the number of circuits to run is $(C_1 + C_2 p)S$, where S is the number of shots, p is the number of ansatz parameters and C_1 , C_2 are constants depending on the cost function estimation method. For, e.g., the Liu21 decomposition, $C_1 = n + 1$ and $C_2 = 2n + 1$. On today's quantum computers, this is a considerable overhead. Thus, for the results in Fig. 6b on a real backend, we only use one ansatz layer and 10 parameter samples (in total 1490 circuits to run S times each). As we can see, the gradient accuracy on `ibmq_montreal` is very poor for C_{N} and much better for C_{NN} . For the latter, we will see in the next section whether this is sufficient for an optimizer to find a good solution.

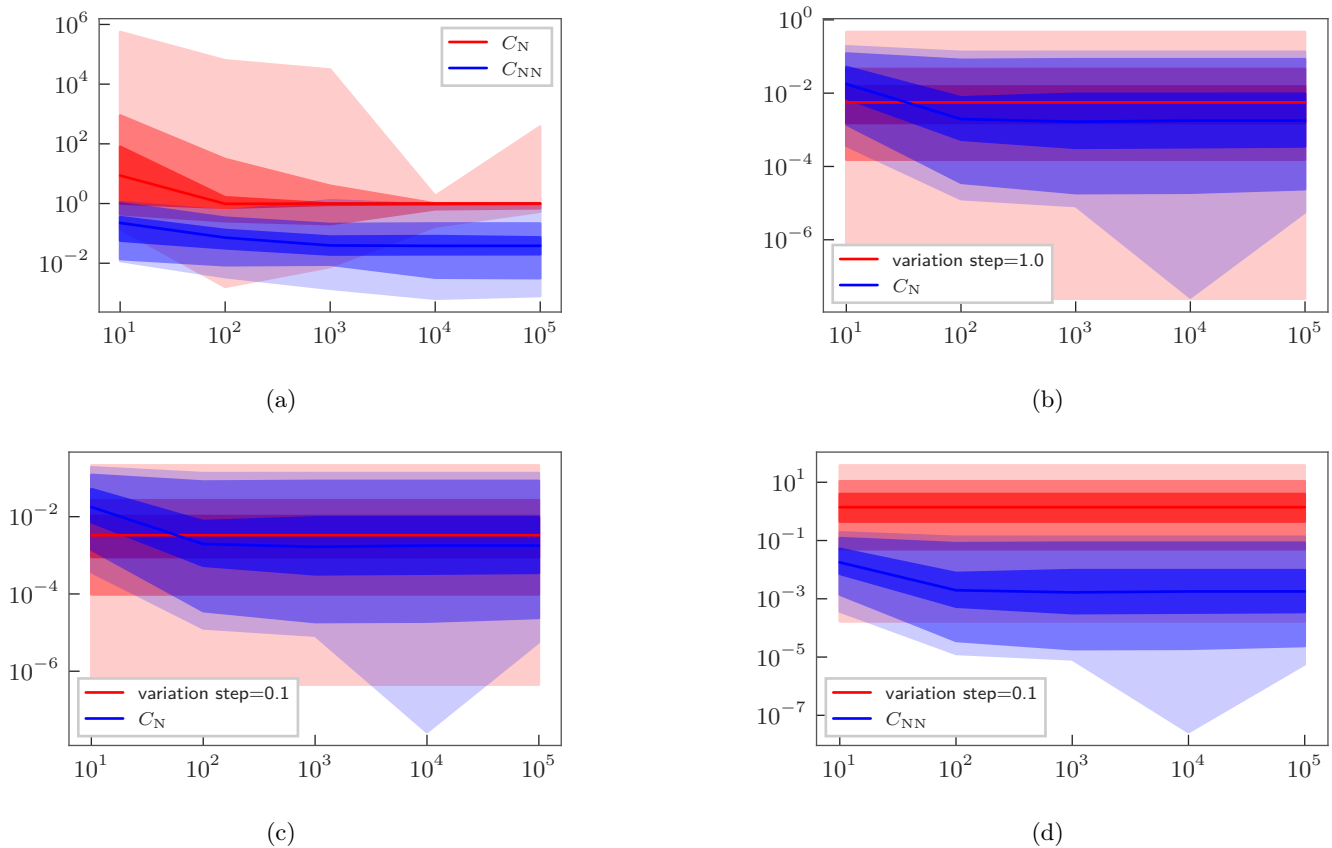


Figure 5: Error percentiles 0, 5, 25, 50, 75, 95 and 100 Linear alternating R_Y - CZ , 5 qubits, 3 layers. (a) Relative error vs. number of shots. (b) – (d) Absolute error vs. number of shots.

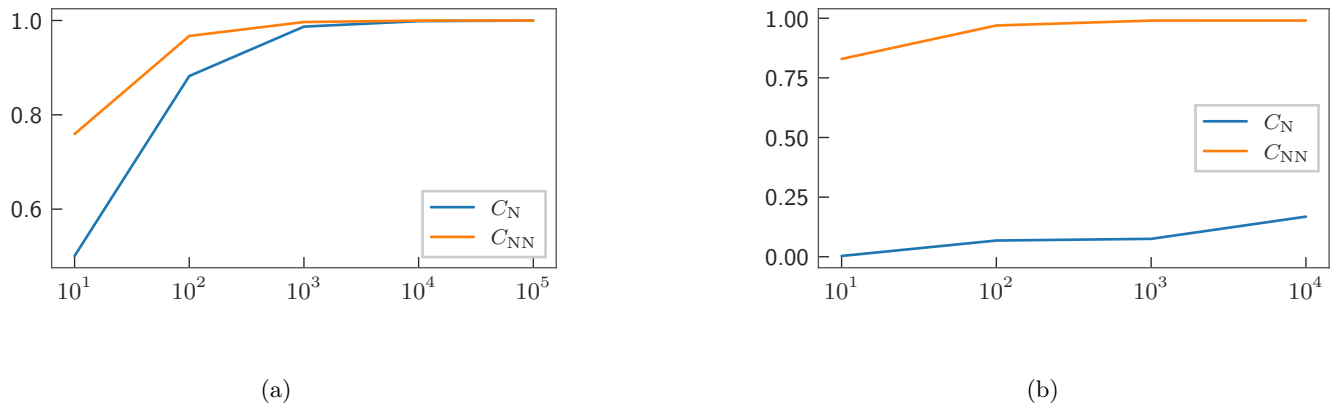


Figure 6: Cosine similarity vs. number of shots for different cost functions. We use the Hadamard test for inner product estimation and the Liu21 decomposition for \mathbf{A} . Linear alternating R_Y - CZ ansatz. (a) Median cosine similarity on a simulator for 50 random parameter samples, 3 layers for the ansatz. (b) Median cosine similarity on `ibmq_montreal` for 10 random parameter samples, 1 layer for the ansatz.

G. Training With Noise

In this section, our VQLS setup consists of a linear alternating R_Y - CZ ansatz with $n = 5$ qubits and $l = 3$ layers ($p = 29$ parameters), RHS (HnX). We have seen

in Section IV A that in this setting the ansatz is capable of representing the solution with near to 100% fidelity. We use the Hadamard test to estimate inner products for both C_N and C_{NN} , and the Liu21 decomposition to estimate $\langle \psi(\theta) | \mathbf{A} | \psi(\theta) \rangle$. We run the experiments on a

simulator with shot noise and the `ibmq_ehningen` backend. We transpile all circuits as mentioned in Section IV B. For results on the quantum device, we present different combinations of transpilation and measurement error mitigation options. Note that we display the fidelity for *all* parameters θ at which the cost was evaluated, i.e., not only for accepted iterates θ_k .

There is a plethora of classical optimizers one could use, many are implemented in `Qiskit` (most are wrappers for the `SciPy` package). Based on the results of Section IV A, other works [29, 35–37] and our own experiments, we only present here the BFGS [25–28], SPSA [38], Powell [39] and NFT [35] optimizers. Other optimizers do not seem to perform better in the presence of hardware noise. Another possible noise-robust candidate – that we did not test here – is the Bayesian optimizer from [40].

In Fig. 7 – 10, we summarize our findings. BFGS performs significantly better for C_{NN} , achieving over 98% fidelity for 10000 shots on a simulator. On a quantum computer, for C_{NN} , BFGS achieves roughly 17% fidelity but does not improve after that. Moreover, the additional cost of evaluating gradients (see also Section IV F) is very time consuming on current quantum hardware: for the linear alternating R_Y - CZ ansatz on 5 qubits with 3 layers and the Liu21 decomposition for \mathbf{A} , one has to run 325 circuits S times to estimate one gradient. The few iterations as displayed in Fig. 7 require hours to execute on `ibmq_ehningen`. Other gradient based methods implemented in `Qiskit` failed to converge even with shot noise only (for a moderate number of shots $S \leq 10^5$).

SPSA does not converge with the default choice of hyperparameters, i.e., using the calibration procedure from [37]. Setting the learning rate to 1, perturbation to 0.1, blocking and trust region to true, we obtain the convergence displayed in Fig. 8. We were not able to find a hyperparameter choice that works on a quantum computer. With QN-SPSA [41], we obtained similar results. SPSA convergence might be improved by an adaptive hyperparameter selection as in, e.g., [42], but we do not investigate this further.

Finally, in Fig. 9 and 10, we present the results for Powell and NFT, respectively. The only tunable hyperparameter for NFT is the reset interval: a smaller interval generally leads to smoother convergence but more cost function evaluations. In this example, we set the reset interval of NFT to 9. On simulators, NFT trained with

C_{NN} performed best, achieving almost 98% fidelity with only 1000 shots per circuit. A similar fidelity was obtained with BFGS trained on C_{NN} with 10000 shots per circuit, at the expense of additionally estimating gradients. On `ibmq_ehningen`, NFT trained on C_{NN} also performed best. Although the maximum observed fidelity was over 80%, the fidelity corresponding to the best observed cost value is only 10.89% (C_{N} trained with no EM). Similar observations about the noise robustness of NFT were made in [35, 36], however, overall, all trainings on quantum devices performed very poorly.

As discussed in the Introduction and Section IV C, we are ultimately interested in estimating inner products with linear functionals. To that end, a more appropriate error metric would be the trace distance. Since we are dealing with pure quantum states, there is a simple relationship between the two

$$\begin{aligned} & \frac{1}{2} \text{tr} \left(\left| |\mathbf{u}\rangle \langle \mathbf{u}| - |\psi(\theta)\rangle \langle \psi(\theta)| \right| \right) \\ & = \sqrt{1 - F(|\mathbf{u}\rangle, |\psi(\theta)\rangle)}, \end{aligned}$$

where $F(|\mathbf{u}\rangle, |\psi(\theta)\rangle)$ is the fidelity between the two pure states. Consequently, a fidelity of 10.89% translates into a trace distance of 0.944, which is a very large error. For convenience, we plot the relationship between fidelity and trace distance in Fig. 11. For a reasonable trace error of $\leq 10^{-1}$, one would require a solution fidelity of at least 99%. This does not include the error of estimating the inner product $\langle r|\psi(\theta)\rangle$ itself.

ACKNOWLEDGEMENTS

This work was supported by the project AnQuC-3 of the Competence Center Quantum Computing Rhineland-Palatinate (Germany). We acknowledge the use of IBM Quantum services for this work. The views expressed are those of the authors, and do not reflect the official policy or position of IBM or the IBM Quantum team.

DATA AVAILABILITY

The results of this work can be reproduced using the code in https://github.com/MazenAli/VQA_Poisson1D.

-
- [1] O. Iliev and V. Laptev, On numerical simulation of flow through oil filters, *Computing and Visualization in Science* **6**, 139 (2004).
- [2] H. Andrä, N. Combaret, J. Dvorkin, E. Glatt, J. Han, M. Kabel, Y. Keehm, F. Krzikalla, M. Lee, C. Madonna, M. Marsh, T. Mukerji, E. H. Saenger, R. Sain, N. Saxena, S. Ricker, A. Wiegmann, and X. Zhan, Digital rock

- physics benchmarks—part ii: Computing effective properties, *Computers & Geosciences* **50**, 33 (2013), benchmark problems, datasets and methodologies for the computational geosciences.
- [3] M. Kabel, T. Böhlke, and M. Schneider, Efficient fixed point and newton–krylov solvers for fft-based homogenization of elasticity at large deformations, *Computa-*

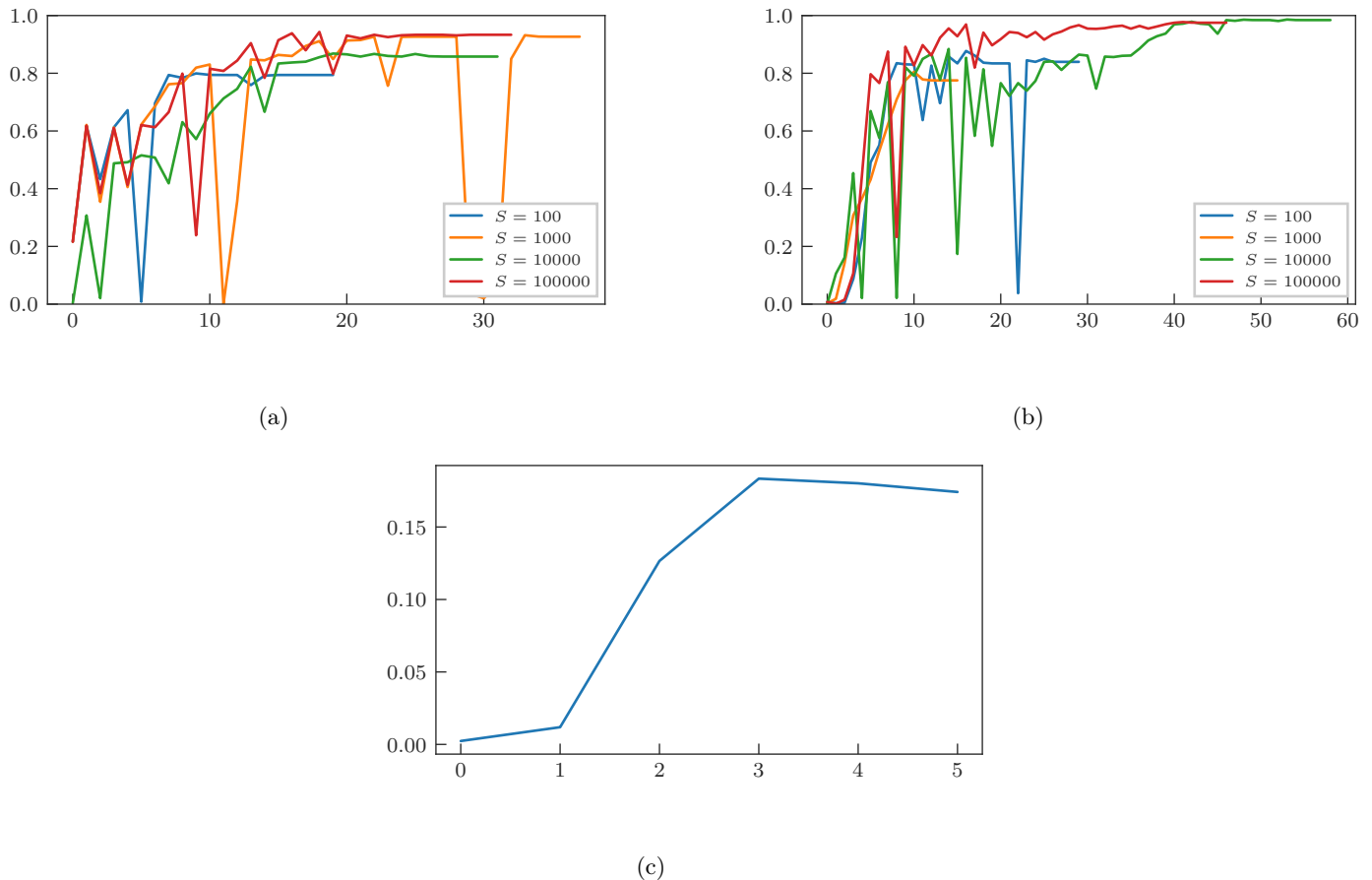
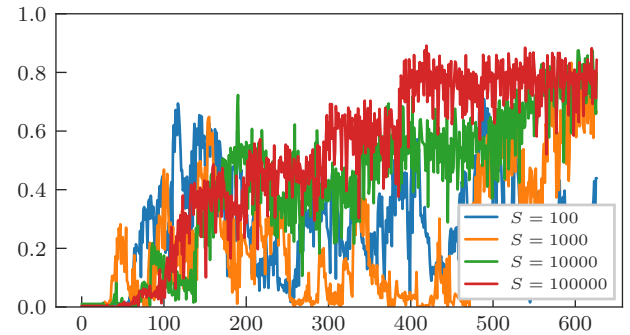
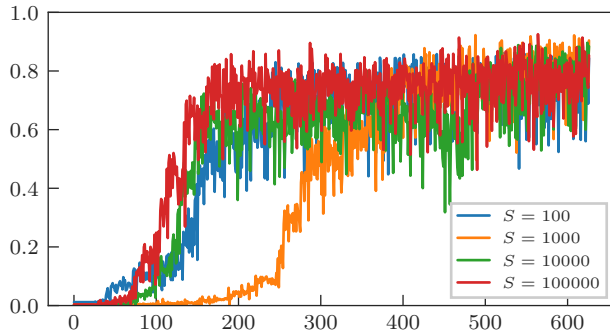
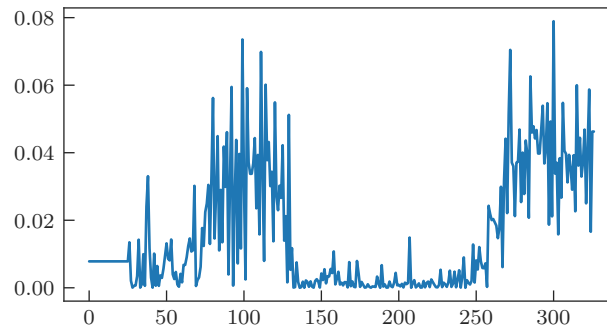


Figure 7: VQLS training on simulators with shot noise and `ibmq_ehningen`, BFGS optimizer with default hyperparameters, linear alternating R_Y - CZ ansatz, 5 qubits and 3 layers, RHS (HnX), Hadamard test for inner product estimation and Liu21 for \mathbf{A} decomposition. (a) Fidelity vs. number of cost function evaluations (gradient evaluations not displayed) on a simulator, training based on C_N . Best out of 15 initial values. (b) Fidelity vs. number of cost function evaluations (gradient evaluations not displayed) on a simulator, training based on C_{NN} . Best out of 15 initial values. (c) Fidelity vs. number of cost function evaluations (gradient evaluations not displayed) on `ibmq_ehningen`, training based on C_{NN} . Optimized noise-aware transpilation with SABRE and `mapomatic`, see also Section IV B, MEM applied, 10000 shots per circuit. Best out of 5 initial values.

- tional Mechanics **54**, 1497 (2014).
- [4] A. W. Harrow, A. Hassidim, and S. Lloyd, Quantum algorithm for linear systems of equations, *Phys. Rev. Lett.* **103**, 150502 (2009).
- [5] A. Montanaro and S. Pallister, Quantum algorithms and the finite element method, *Phys. Rev. A* **93**, 032324 (2016).
- [6] K. K. Saha, W. Robson, C. Howington, I.-S. Suh, Z. Wang, and J. Nabrzycki, Advancing Algorithm to Scale and Accurately Solve Quantum Poisson Equation on Near-term Quantum Hardware, arXiv e-prints, arXiv:2210.16668 (2022), arXiv:2210.16668 [quant-ph].
- [7] W. Robson, K. K. Saha, C. Howington, I.-S. Suh, and J. Nabrzycki, Advanced Quantum Poisson Solver in the NISQ era, arXiv e-prints, arXiv:2209.09366 (2022), arXiv:2209.09366 [quant-ph].
- [8] A. C. Vazquez, R. Hiptmair, and S. Woerner, Enhancing the quantum linear systems algorithm using richardson extrapolation, *ACM Transactions on Quantum Computing* **3**, 10.1145/3490631 (2022).
- [9] M. Cerezo, A. Arrasmith, R. Babbush, S. C. Benjamin, S. Endo, K. Fujii, J. R. McClean, K. Mitarai, X. Yuan, L. Cincio, and P. J. Coles, Variational quantum algorithms, *Nature Reviews Physics* **3**, 625 (2021).
- [10] Y. Sato, R. Kondo, S. Koide, H. Takamatsu, and N. Imoto, Variational quantum algorithm based on the minimum potential energy for solving the poisson equation, *Phys. Rev. A* **104**, 052409 (2021).
- [11] H.-L. Liu, Y.-S. Wu, L.-C. Wan, S.-J. Pan, S.-J. Qin, F. Gao, and Q.-Y. Wen, Variational quantum algorithm for the poisson equation, *Phys. Rev. A* **104**, 022418 (2021).
- [12] R. Demirdjian, D. Gunlycke, C. A. Reynolds, J. D. Doyle, and S. Tafur, Variational quantum solutions to the advection-diffusion equation for applications in fluid dynamics, *Quantum Information Processing* **21**, 322 (2022).
- [13] C. Bravo-Prieto, R. LaRose, M. Cerezo, Y. Subasi, L. Cincio, and P. J. Coles, Variational Quantum Lin-



(a)



(b)

Figure 8: VQLS training on simulators with shot noise and `ibmq_ehningen`, SPSA optimizer with learning rate 1, perturbation 0.1, blocking and trust region set, linear alternating R_Y - CZ ansatz, 5 qubits and 3 layers, RHS (HnX), Hadamard test for inner product estimation and Liu21 for \mathbf{A} decomposition. (a) Fidelity vs. number of cost function evaluations on a simulator, training based on C_N . Best out of 15 initial values. (b) Fidelity vs. number of cost function evaluations on a simulator, training based on C_{NN} . Best out of 15 initial values. (c) Fidelity vs. number of cost function evaluations on `ibmq_ehningen`, training based on C_{NN} . Optimized noise-aware transpilation with SABRE, no MEM applied, 1000 shots per circuit. Best out of 5 initial values.

ear Solver, arXiv e-prints , arXiv:1909.05820 (2019), arXiv:1909.05820 [quant-ph].

- [14] IBM Quantum. <https://quantum-computing.ibm.com/>, 2022.
- [15] Nonetheless, other issues may render VQLS unusable, e.g., high number of variational parameters or exponentially worse barren plateaus. Moreover, the convergence rate of the estimation error w.r.t. the number of shots is at best square root, i.e., analogous to classical Monte Carlo methods.
- [16] J. Sirignano and K. Spiliopoulos, Dgm: A deep learning algorithm for solving partial differential equations, *Journal of Computational Physics* **375**, 1339 (2018).
- [17] J. Han, A. Jentzen, and W. E, Solving high-dimensional partial differential equations using deep learning, *Proceedings of the National Academy of Sciences* **115**, 8505 (2018), <https://www.pnas.org/doi/pdf/10.1073/pnas.1718942115>.
- [18] M. Bachmayr, R. Schneider, and A. Uschmajew, Tensor networks and hierarchical tensors for the solution of high-dimensional partial differential equations, *Foundations of Computational Mathematics* **16**, 1423 (2016).
- [19] K. Temme, S. Bravyi, and J. M. Gambetta, Error mitigation for short-depth quantum circuits, *Phys. Rev. Lett.* **119**, 180509 (2017).
- [20] E. van den Berg, Z. K. Mineev, A. Kandala, and K. Temme, Probabilistic error cancellation with sparse Pauli-Lindblad models on noisy quantum processors, arXiv e-prints , arXiv:2201.09866 (2022), arXiv:2201.09866 [quant-ph].
- [21] By convention, the measurements on a quantum device are performed in the Z -basis. Therefore, we require an H -gate to rotate into the X -basis.
- [22] A. Peruzzo, J. McClean, P. Shadbolt, M.-H. Yung, X.-Q. Zhou, P. J. Love, A. Aspuru-Guzik, and J. L. O’Brien, A variational eigenvalue solver on a photonic quantum processor, *Nature Communications* **5**, 4213 (2014).
- [23] M. Cerezo, A. Sone, T. Volkoff, L. Cincio, and P. J. Coles, Cost function dependent barren plateaus in shallow parametrized quantum circuits, *Nature Communica-*

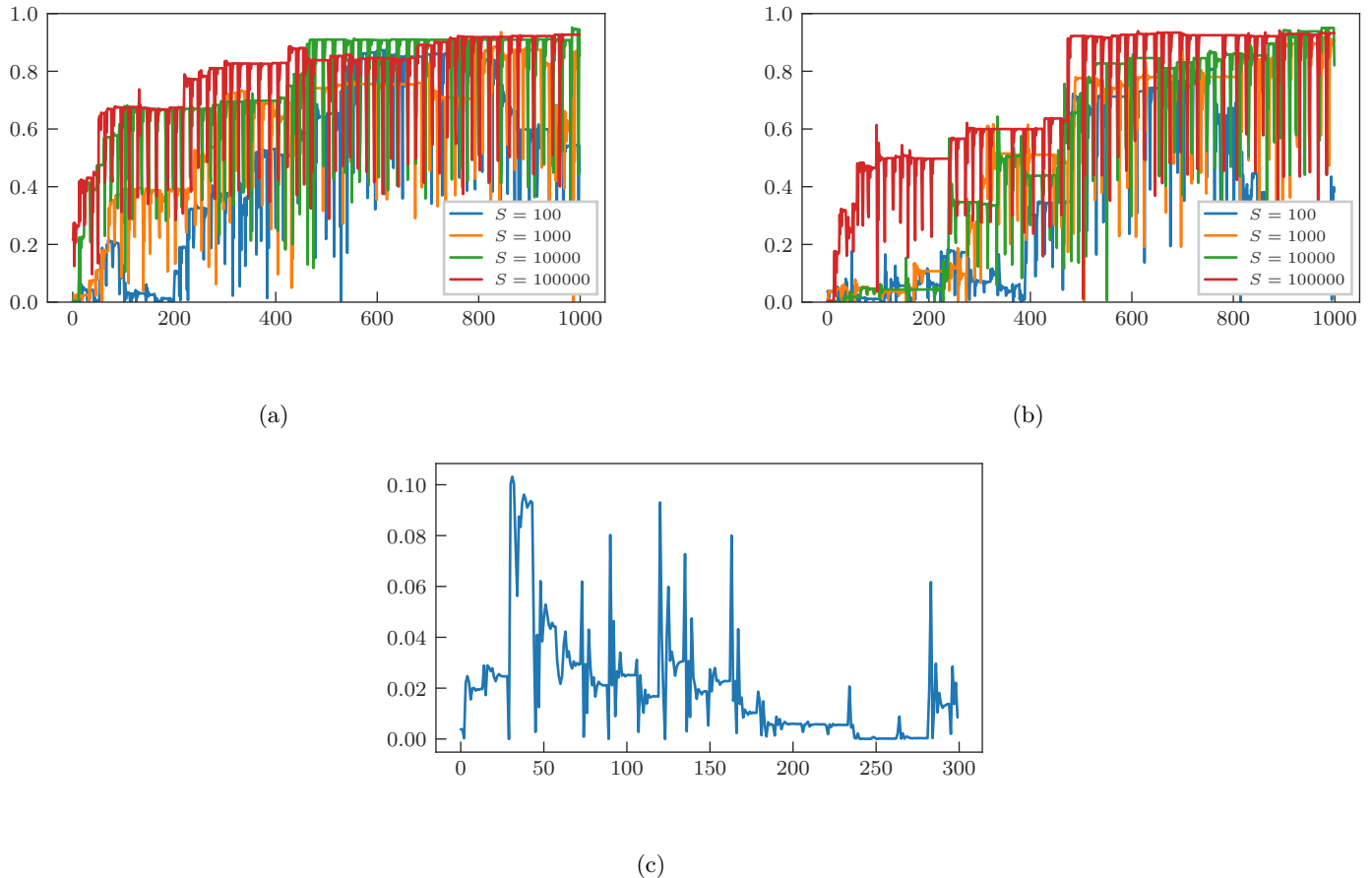


Figure 9: VQLS training on simulators with shot noise and `ibmq_ehningen`, POWELL optimizer with default hyperparameters, linear alternating R_Y - CZ ansatz, 5 qubits and 3 layers, RHS (HnX), Hadamard test for inner product estimation and Liu21 for \mathbf{A} decomposition. (a) Fidelity vs. number of cost function evaluations on a simulator, training based on C_N . Best out of 15 initial values. (b) Fidelity vs. number of cost function evaluations on a simulator, training based on C_{NN} . Best out of 15 initial values. (c) Fidelity vs. number of cost function evaluations on `ibmq_ehningen`, training based on C_{NN} . Optimized noise-aware transpilation with SABRE, no MEM applied, 10000 shots per circuit. Best out of 5 initial values.

- tions **12**, 1791 (2021).
- [24] M. Cerezo, K. Sharma, A. Arrasmith, and P. J. Coles, Variational quantum state eigensolver, *npj Quantum Information* **8**, 113 (2022).
- [25] C. G. Broyden, The Convergence of a Class of Double-rank Minimization Algorithms: 2. The New Algorithm, *IMA Journal of Applied Mathematics* **6**, 222 (1970), <https://academic.oup.com/imamat/article-pdf/6/3/222/1848059/6-3-222.pdf>.
- [26] R. Fletcher, A new approach to variable metric algorithms, *The Computer Journal* **13**, 317 (1970), <https://academic.oup.com/comjnl/article-pdf/13/3/317/988678/130317.pdf>.
- [27] D. Goldfarb, A family of variable-metric methods derived by variational means, *Mathematics of Computation* **24**, 23 (1970).
- [28] D. F. Shanno, Conditioning of quasi-newton methods for function minimization, *Mathematics of Computation* **24**, 647 (1970).
- [29] A. Pellow-Jarman, I. Sinayskiy, A. Pillay, and F. Petruccione, A comparison of various classical optimizers for a variational quantum linear solver, *Quantum Information Processing* **20**, 202 (2021).
- [30] Recently, IBM extended their software tools by adding runtime primitives with streamlined error mitigation. Some noteworthy error mitigation techniques not considered in our tests are zero noise extrapolation and probabilistic error cancellation [19, 20].
- [31] G. Li, Y. Ding, and Y. Xie, Tackling the qubit mapping problem for nisq-era quantum devices, in *Proceedings of the Twenty-Fourth International Conference on Architectural Support for Programming Languages and Operating Systems*, ASPLOS '19 (Association for Computing Machinery, New York, NY, USA, 2019) p. 1001–1014.
- [32] P. D. Nation, H. Kang, N. Sundaresan, and J. M. Gambetta, Scalable mitigation of measurement errors on quantum computers, *PRX Quantum* **2**, 040326 (2021).
- [33] P. D. Nation and M. Treinish, Suppressing quantum circuit errors due to system variability, arXiv e-prints ,

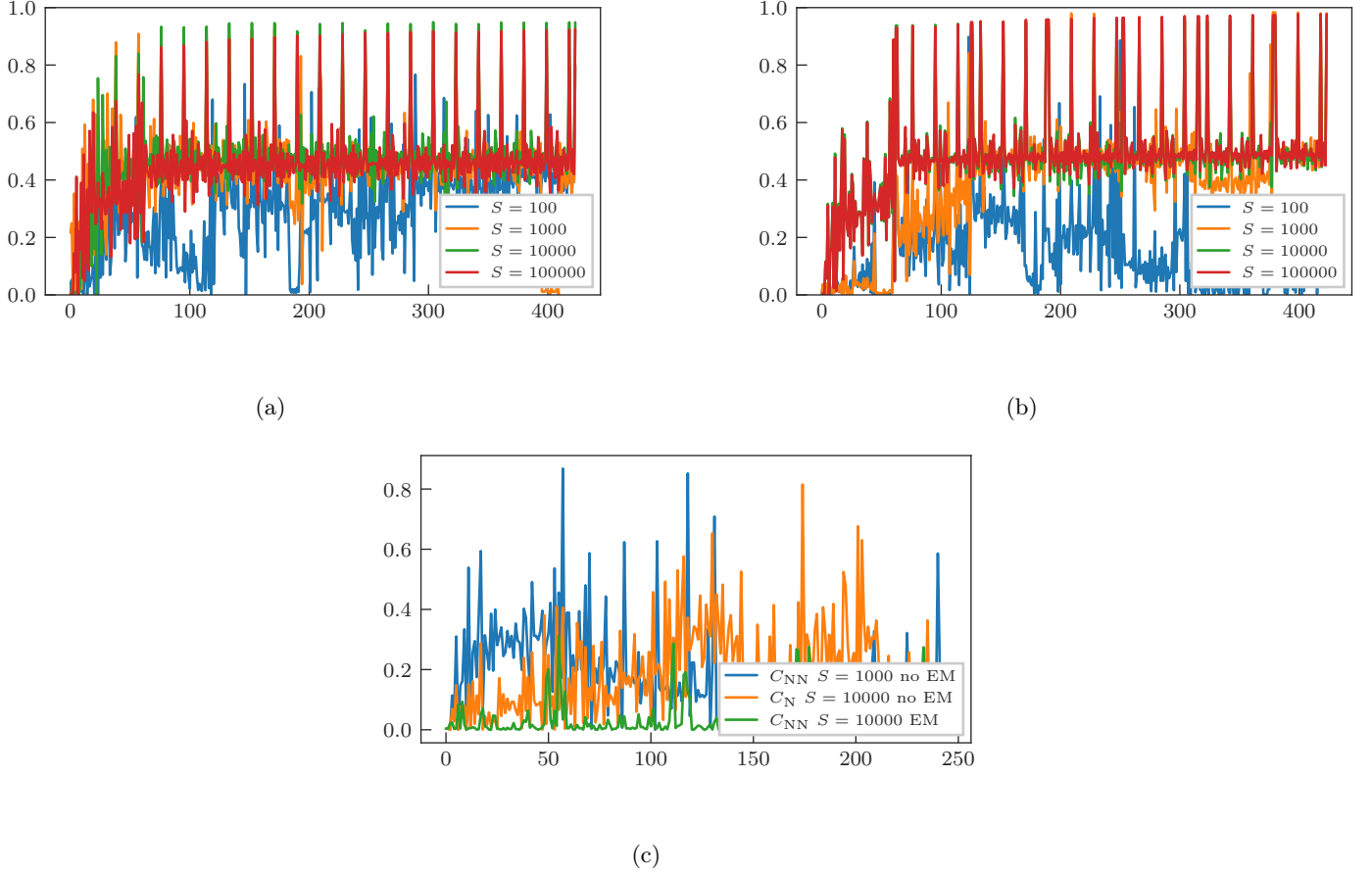


Figure 10: VQLS training on simulators with shot noise and `ibmq_ehningen`, NFT optimizer with reset interval 9, linear alternating R_Y - CZ ansatz, 5 qubits and 3 layers, RHS (HnX), Hadamard test for inner product estimation and Liu21 for \mathbf{A} decomposition. (a) Fidelity vs. number of cost function evaluations on a simulator, training based on C_N . Best out of 15 initial values. (b) Fidelity vs. number of cost function evaluations on a simulator, training based on C_{NN} . Best out of 15 initial values. (c) Fidelity vs. number of cost function evaluations on `ibmq_ehningen`. “No EM” means only optimized transpilation with SABRE and “EM” means additionally noise-aware transpilation with `mapomatic` and MEM. Best out of 5 initial values.

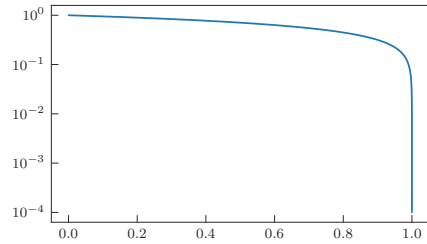


Figure 11: Trace distance (y -axis) vs. fidelity (x -axis). The last point on the x -axis is 0.99999999.

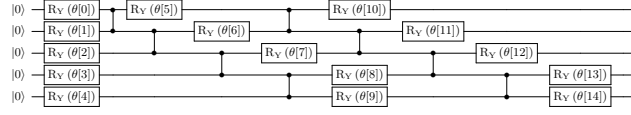
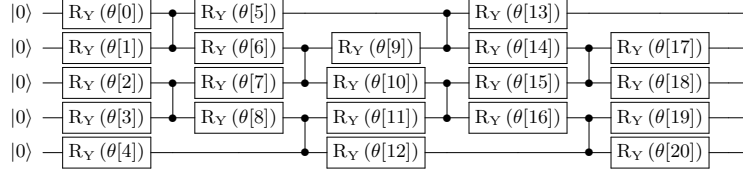
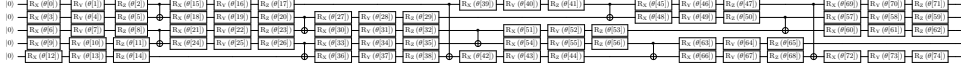
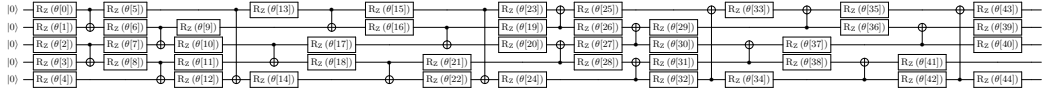
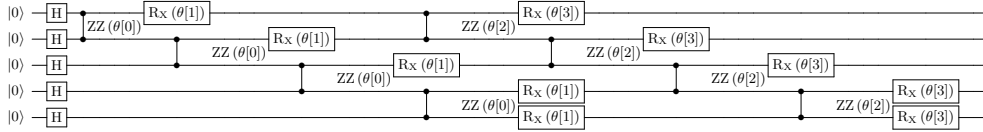
arXiv:2209.15512 (2022), arXiv:2209.15512 [quant-ph].

[34] G. Ravi, K. N. Smith, P. Gokhale, A. Mari, N. Earnest, A. Javadi-Abhari, and F. T. Chong, Vaqem: A variational approach to quantum error mitigation, in *2022 IEEE International Symposium on High-Performance Computer Architecture (HPCA)* (IEEE Computer Society, Los Alamitos, CA, USA, 2022) pp. 288–303.

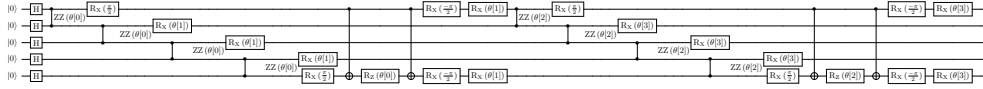
[35] K. M. Nakanishi, K. Fujii, and S. Todo, Sequential minimal optimization for quantum-classical hybrid algorithms, *Phys. Rev. Research* **2**, 043158 (2020).

[36] M. Oliv, A. Matic, T. Messerer, and J. M. Lorenz, Evaluating the impact of noise on the performance of the Variational Quantum Eigensolver, arXiv e-prints , arXiv:2209.12803 (2022), arXiv:2209.12803 [quant-ph].

- [37] A. Kandala, A. Mezzacapo, K. Temme, M. Takita, M. Brink, J. M. Chow, and J. M. Gambetta, Hardware-efficient variational quantum eigensolver for small molecules and quantum magnets, *Nature* **549**, 242 (2017).
- [38] J. Spall, Accelerated second-order stochastic optimization using only function measurements, in *Proceedings of the 36th IEEE Conference on Decision and Control*, Vol. 2 (1997) pp. 1417–1424 vol.2.
- [39] M. J. D. Powell, An efficient method for finding the minimum of a function of several variables without calculating derivatives, *The Computer Journal* **7**, 155 (1964), <https://academic.oup.com/comjnl/article-pdf/7/2/155/959784/070155.pdf>.
- [40] G. Iannelli and K. Jansen, Noisy Bayesian optimization for variational quantum eigensolvers, *PoS LATTICE2021*, 251 (2022), arXiv:2112.00426 [quant-ph].
- [41] J. Gacon, C. Zoufal, G. Carleo, and S. Woerner, Simultaneous Perturbation Stochastic Approximation of the Quantum Fisher Information, *Quantum* **5**, 567 (2021).
- [42] S. H. Sack, R. A. Medina, A. A. Michailidis, R. Kueng, and M. Serbyn, Avoiding barren plateaus using classical shadows, *PRX Quantum* **3**, 020365 (2022).

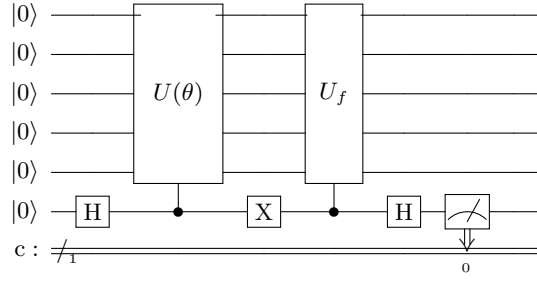
(a) Linear R_Y - CZ , 5 qubits, 2 layers.(b) Linear alternating R_Y - CZ , 5 qubits, 2 layers.(c) Linear alternating periodic $U3$ - CX , 5 qubits, 2 layers.(d) Linear alternating periodic bidirectional R_Z - CX , 5 qubits, 2 layers.

(e) QAOA (inspired) ansatz, 5 qubits, 2 layers.

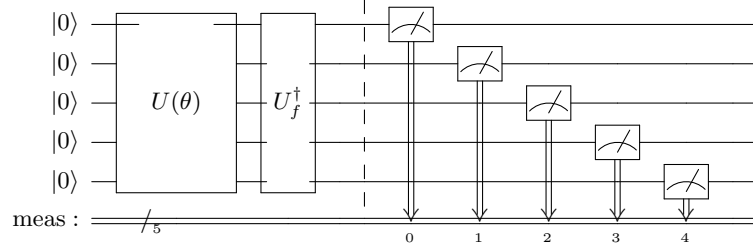


(f) QAOA periodic, 5 qubits, 2 layers.

Figure 12: Ansatzes used for $|\psi(\theta)\rangle$ in this work.



(a) Hadamard test for estimating $\Re \langle \mathbf{f} | \psi(\theta) \rangle$.



(b) Overlap test for estimating $|\langle \mathbf{f} | \psi(\theta) \rangle|^2$.

Figure 13: Circuits for estimating inner products with $|\psi(\theta)\rangle = U(\theta) |0\rangle$ and $|\mathbf{f}\rangle = U_f |0\rangle$.

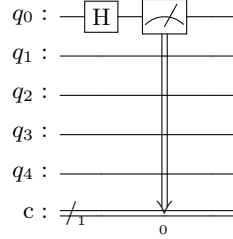


Figure 14: Circuit for $I^{\otimes n-1} \otimes X$ required for all decompositions.

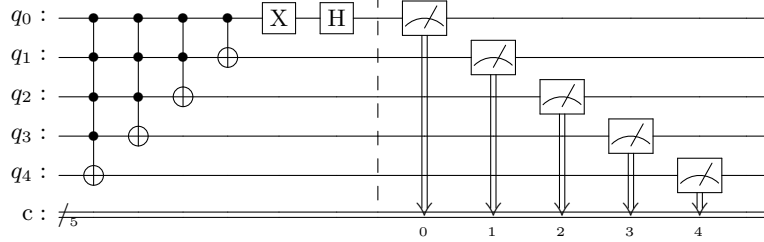


Figure 15: Sato21: circuit for estimating expectation of \mathbf{A} as in [10].

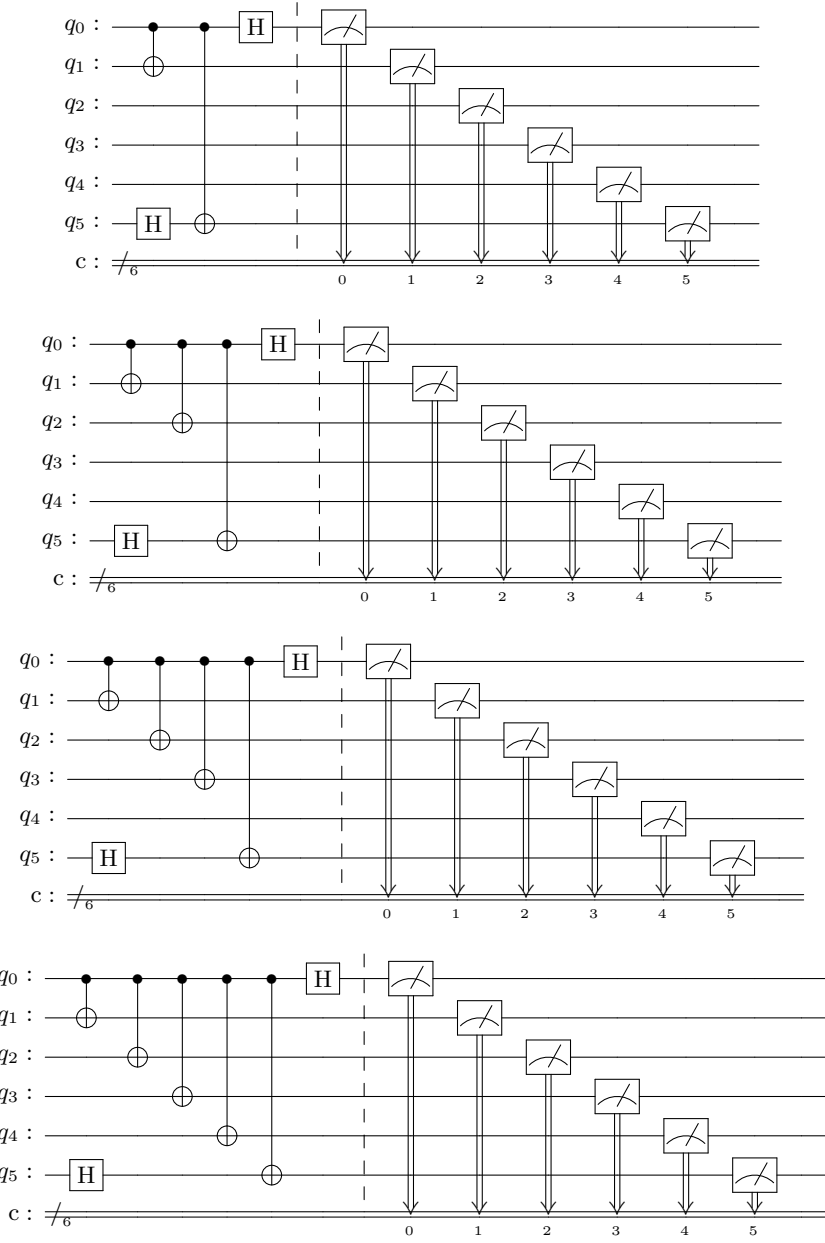


Figure 16: Liu21: circuits for estimating expectation of \mathbf{A} as in [11].

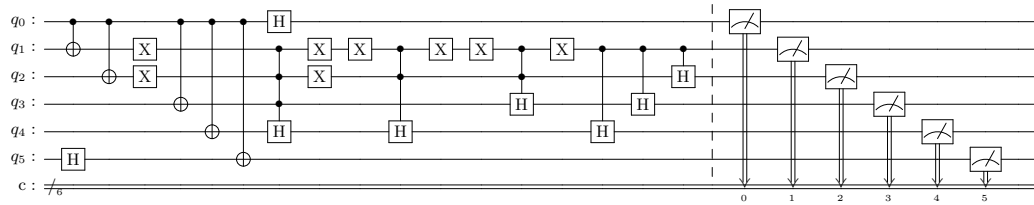
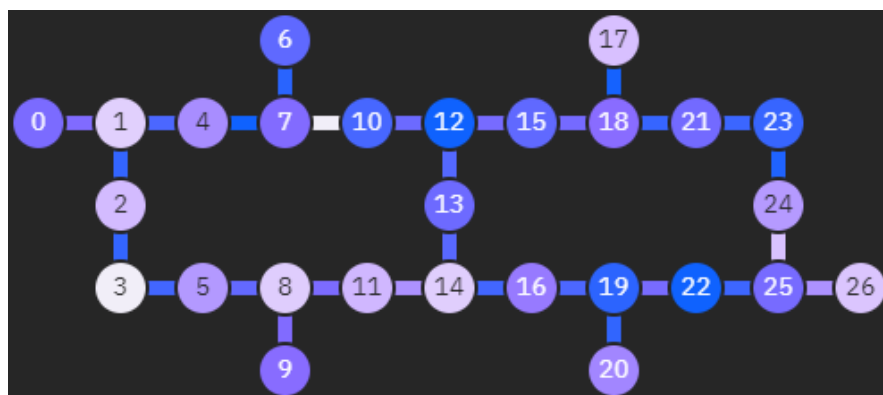
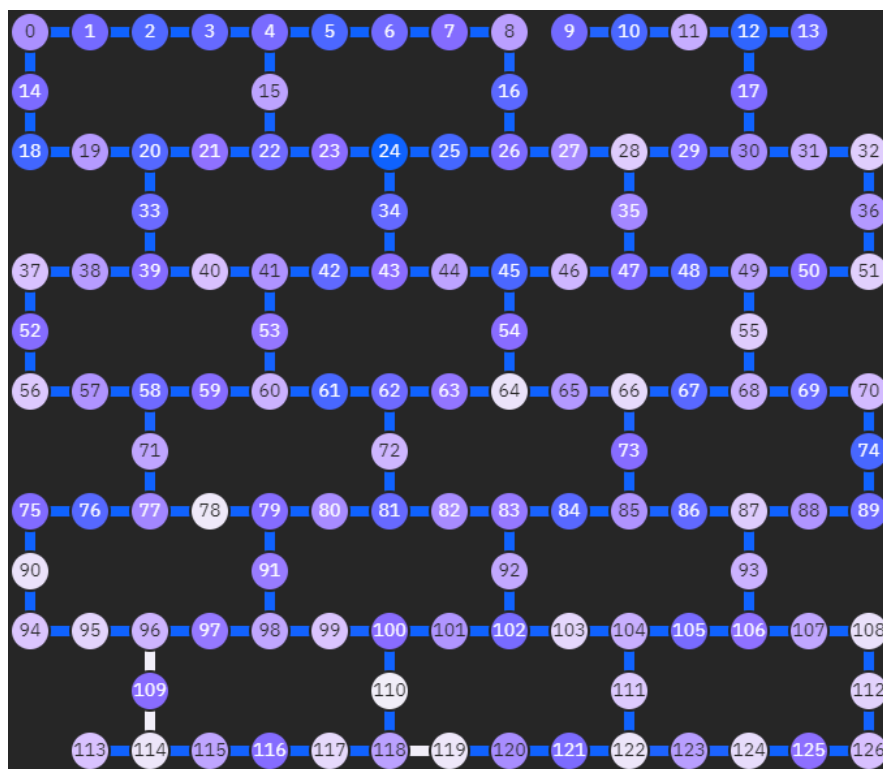


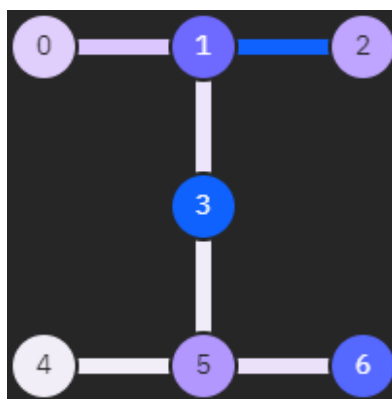
Figure 17: Liu21Grouped: circuit for rotating into the common eigenbasis of the commuting operators proposed in [11].



(a)



(b)



(c)

Figure 18: Examples of IBM backend connectivity maps (from (a) to (c)): `ibmq_ehningen`, `ibmq_washington` and `ibmq_lagos`. Lighter nodes/connections means a larger error.